npj | computational materials

Article

Published in partnership with the Shanghai Institute of Ceramics of the Chinese Academy of Sciences

https://doi.org/10.1038/s41524-024-01348-w

High pressure suppression of plasticity due to an overabundance of shear embryo formation

Brenden W. Hamilton ✉ & Timothy C. Germann

High pressure shear band formation is a critical phenomenon in energetic materials due to its influence on both mechanical strength and mechanochemical activation. While shear banding is known to occur in a variety of these materials, the governing dynamics of the mechanisms are not well defined for molecular crystals. We conduct molecular dynamics simulations of shock wave induced shear band formation in the energetic material 1,3,5-trinitroperhydro-1,3,5-triazine (RDX) to assess shear band nucleation processes. We find, that at high pressures, the initial formation sites for shear bands, "embryos", form in excess and rapidly lower deviatoric stresses prior to shear band formation and growth. This results in the suppression of plastic deformation. A local cluster analysis is used to quantify and contrast this mechanism with a more typical shear banding seen at lower pressures. These results demonstrate a mechanism that is reversible in nature and that supersedes shear band formation at increased pressures. We anticipate that these results will have a broad impact on the modeling and development of high-strain rate application materials such as those for high explosives and hypersonic systems.

Shear bands, regions of localized plasticity induced from high shear stresses, form to accommodate further deformation in materials and can lead to the buildup of material damage, as well as a potential decrease in flow stress[1]. Shear banding has been known to occur in a variety of materials classes, including crystalline metals[2–4], ceramics[5–7], metallic glasses[8–14], and molecular materials[15–17].

Overall, shear banding generally occurs when there is a local shear induced softening of the material, creating regions that are much more susceptible to a rapid material flow[9]. This leads to a localized, plastic instability that lowers the deviatoric stress components of the material and allows for continued deformation. Shear banding has been of more recent interest due to its relevance in metallic glasses, as well as the observance of shear band formation without prior defect accumulation[18]. In the latter case, these shear bands were found to allow for continued deformation in the absence of dislocations without inducing cavitation or material failure.

A recent study has shown that shear bands nucleate to accommodate deformation (without defect accumulation) when the material has a low difference in energy between the crystal and amorphous phases, such that forming amorphous bands is energetically favorable to other mechanisms[2]. Shear banding sans crystalline defects is also well studied in polymers, in which glassy and entangled molecules can flow, even below the glass transition state[17,19]. Molecular solids, which are often utilized at ultra-high-strain rates such as shock loading, pose a grand challenge in studying shear band formation due to their complex crystal packing and limited crystalline defect formation mechanisms. The processes of initial shear band nucleation in molecular crystals is not well defined.

Under shock loading, shear banding is a common plastic deformation mechanism for a wide range of materials[20,21]. As the shock uniaxially deforms the material at an extremely high-strain rate ($\geq 10^9$/s) to a high pressure deviatoric state, plastic events such as shear banding can occur on picosecond timescales, directly behind the shock front. Often, experimentally observing these phenomena proves difficult due to the time and length scales involved, especially for time resolved processes[22–27]. However, recent advances in ultrafast, in situ capabilities have begun to make the experimental probing of these processes in real time at the nanoscale more of a reality[28–30]. These experimental setups are poised to be directly comparable to molecular dynamics simulations large enough to resolve these phenomena.

In general, for energetic materials, shear bands can induce a mechanochemical acceleration of kinetics[21,31,32], making shear banding a highly relevant and complex chemical initiation mechanism. Mechanochemistry in energetic molecular solids typically occurs via a shock wave creating large intra-molecular strains via local material flow[33–37]. These strains then lead to a lowered activation barrier and accelerated kinetics in areas such as pore collapses and shear bands[38–41], and they can occur in other materials such as graphite[42,43] and mechanophores[44,45].

Theoretical Division, Los Alamos National Laboratory, Los Alamos, NM, 87545, USA. ✉e-mail: brenden@lanl.gov

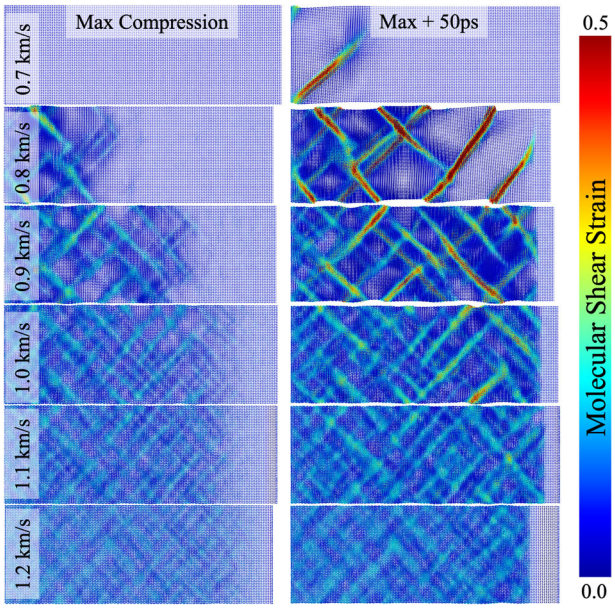

Fig. 1 | Molecular renderings of the X–Z plane for the time of maximum compression (left) and 50 ps later, held at that compression (right), molecules are colored by the shear strain (von Mises invariant of the Green-Lagrange strain tensor). A figure of the same frames with a narrower color bar range is available in Supplementary Fig. 1.

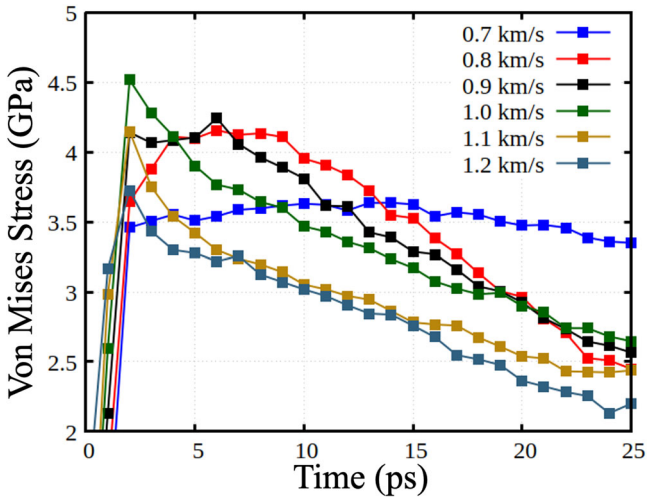

Fig. 2 | Time history of the von Mises stress of a 1D slice of material at 10.0 to 12.5 nm from the piston for all particle velocities.

Here, we study shear banding in a molecular crystal, specifically the energetic material 1,3,5-trinitroperhydro-1,3,5-triazine (RDX). Shear banding is known to occur in RDX[15], and occurs due to local thermal softening, not defect buildup[46]. These shear bands can form out of regions that initially show a rise in molecular conformation changes that leads to local softening[47], and the associated free energy changes are indicative of a local first-order structural phase transition[47]. These initial shear nucleation "embryos" can grow or agglomerate to shear band nuclei which are driven to continue growing under shear stress loads. Here, we show an additional mechanism in which higher pressure shear bands are suppressed due to an over-formation of shear embryos that lowers the deviatoric stress enough to prevent the formation of critical nuclei. This rapidly reduces the driving force for shear band growth and no significant plasticity occurs at higher pressures, in contrast to the significant plasticity seen at lower shock pressures where fewer embryos form.

Results

Shock compression

We conduct shock compression simulations using all-atom molecular dynamics, compressing RDX along the [100] crystal direction for particle velocities (U_p) ranging from 0.7 to 1.2 km/s. Figure 1 shows molecular (center of mass) renderings of these simulations, colored by the molecular shear strain (von Mises invariant of the Green-Lagrange strain tensor), at both the time of maximum compression when the shockwave reaches the far surface, and 50ps later, with the system held at maximum compression using shock absorbing boundary conditions (SABCs)[15,35,48]. These SABCs force the system to a static compression state, held at shock conditions and preventing any release. This is akin to quenching a dynamic system to catch it at a specific moment in the process and assess it. Here, the SABCs hold the material at the increased temperature and pressure of the shock for an indefinite amount of time.

These localizations of shear strain, in all cases, form a band-like structure. For the weaker shock strengths, this manifests in a few thin bands of high shear strain, "shear bands", illustrated by the orange and red regions in Fig. 1. Conversely, in the stronger shock cases, where resolved shear stresses are heightened, leading to a higher driving force for shear deformation, the shear strain localizations strikingly lack intensity, but are also considerably more pervasive. Supplementary Fig. 4 presents a 1D binning (along the shock direction) of the shear strain, displaying that the stronger shock cases result in a greater average shear strain per molecule (or volume), despite a lack of appreciable shear banding. It should be noted that, for the shear band case, the average shear strain is taken over the bifurcated state of the material where a significant majority is un-deformed crystal, as compared to the amorphous shear bands. In the stronger shock cases, running the simulation for significantly longer times does not result in more localized shear or any shear band formation, such that, by 50ps after maximum compression, the system strain is predominately static, regarding any continual structural evolution (see Supplementary Fig. 3 for a 450 ps hold the shows the same).

Hence, here we observe conditions in which the lower pressure systems exhibit significant, localized plasticity, however, increases in the uniaxial compression rate, leading to more shear stress, results in little to no plasticity, just a nominal shear deformation to a significant number of molecules, suppressing plasticity with increasing pressure. Additionally, for the weaker shocks, the shear banding occurs significantly behind the shock front, whereas the more homogeneous deformation of the stronger shock cases occurs nearly adjacent to the rise in pressure from the shock. Furthermore, these stronger shock cases result in the retainment of the crystal structure throughout, not a localized plasticity event.

Figure 2 shows a time history of the von Mises (VM) stress for a planar slice of material 2.5 nm wide, beginning at 10.0 nm from the piston. For 0.7 km/s, which does not shear band in the time of the shock passage of the entire sample, which is 24 ps for this case, the VM stress does not significantly change. Shifting to the prompt shear banding cases of 0.8 and 0.9 km/s, the VM stress sits at its peak value for 5–10 ps, before slowly decaying as plasticity begins to materialize, resulting in a much more hydrostatic state during the maximum compression hold.

For the strongest shock cases, a rapid decrease in VM stress is observed, occurring on the timescale of the shock rise, decreasing so promptly that the peak value shown lowers with rising shock strength. However this is an artificial smoothing due to the bin size and temporal spacing of the points, where material in the upstream side of the bin commences decaying its VM stress prior to total compression of the bin. This rapid decrease occurs, sans plasticity of any meaningful quantity, and the driving force for shear band formation, large deviatoric stresses, fails to be sustained in a requisite intensity to induce shear band formation. Hence, this deformation mechanism usurps the shear banding mechanism and nullifies the driving force before significant plasticity can occur. As an analogy, in solidification, the formation of a higher number of crystal embryos leads to considerable

nucleation sites, which results in smaller grain sizes. Here, for strong shocks, we see an excess of "shear embryos" form. However, these begin the lower the driving force for "growth" (VM stress). Instead of altering the structure of final state like in solidification, here, an excess of embryos entirely arrests the process. Here, the formation of shear embryos lowers the VM stress, resulting in the release of a significant fraction of the stored energy in shear from uniaxial compression. This allows the system to evolve toward a more hydrostatic state without the need to induce any plastic flow.

Rapid VM stress decays, like that shown here for strong shocks, may also indicate a phase transformation. Based on experimental phase diagrams[49] for RDX, all the states studied here should exist in the γ phase (the highest shock temperature reached here is 420 K). Supplementary Fig. 6 shows radial distribution function g(r) curves for the initial state and all shocked states, further showing that no phase transition occurs at the stronger shocks, relative to the weaker shocks. Supplementary Fig. 7 also presents maps of molecular rotations, showing that no other explicit phase change mechanism is occurring.

Shock release

Figure 3 shows molecular renderings of a release of the SABCs, permitting the material to expand back toward ambient density, for a shear band and high pressure no shear band case, 0.8 and 1.1 km/s, respectively. The SABC on the downstream face of the material is lifted after 50 ps of continuous compression, and the material begins to uniaxially expand in a rarefaction process. In the 0.8 km/s case, the shear bands neither recover to a crystalline phase nor initiate failure via void formation/cavitation. The shear bands persist throughout the total release of the material (bottom row, +80 ps) and continue to exhibit some strength and binding of the material.

Conversely, with the 1.1 km/s case, the regions of deformation, which can be discerned as the regions of increased color/darkness due to obfuscation of the white background, present an entirely alternative release response. As the release wave alleviates the latent stress of the compressed system, a substantial majority of these local deformations undergo an annealing-like processes and reverts to the original crystal structure. This shows that the existence of the "shear embryos" is only supported by the pressure/shear state and is not a local energy minimum that is metastable at lower pressure. Supplementary Fig. 8 shows the decrease rate in sheared molecules for both cases in Fig. 3. These results further propound the idea of plasticity suppression at higher shock strengths, such that the release wave rapidly eliminates the presence of sheared molecules in the 1.1 km/s case.

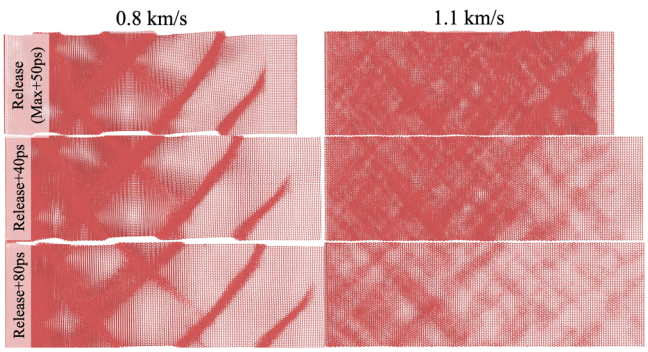

Fig. 3 | Molecular center of mass renderings for the release of the compressed systems, starting from 50 ps after maximum compression, until full release, for the 0.8 and 1.1 km/s cases.

Overall, this reveals the high pressure mechanism to be reversible in nature, and, therefore, by definition, non-plastic. This non-plastic shear deformation occurs at high enough density and has broad enough spatial tendencies to drive down the local deviatoric stresses enough to suppress plasticity, preventing the embryo from overcoming the high barrier for shear band nucleation and growth. We spend the rest of this work attempting to characterize this high pressure mechanism.

Cluster and correlation analysis

To arbitrarily classify and study only the highly sheared regions of the material, we remove all molecules that have a shear strain of less than 0.15. Figure 4 displays molecular renderings of this reduced system at 50 ps after maximum compression. The weaker shocks (top row) develop clear bands of amorphous material that span the width of the sample and consist of both "upwards" and "downwards" propagating shear bands. These bands interweave with one another to form a shear band network. By 1.0 km/s, these bands begin to increase in density sufficiently such that they begin to coalesce, resulting in a less defined network structure.

In the 1.1 and 1.2 km/s cases, no well-defined structure of the sheared material exists, and the magnitude of the shear strain is considerably lower on average. For these cases, sheared material appears rapidly at the shock front, en masse, but never forms the defined bands of the weaker shock cases. This is due to an overabundance of shear embryos that never grow into critical nuclei for shear banding, and instead generally retain their crystallinity. Small amounts of molecules in various locations begin to shear, just as occurs for the shear bands that nucleate in the weaker shocks. However, the number of these embryos is far greater and they occur much closer to the shock front. This rapidly lowers the VM stress (as shown in Fig. 2) and reduces the driving force for the shear band nucleation, preventing the embryos sites from growing into shear band nucleation sites, suppressing the formation of plasticity.

Supplementary Fig. 9 has heat map plots of the XZ Component of the Deformation Gradient Tensor (Green-Lagrange) vs. the Shear Strain, in which the shear band cases show significant structure, but the suppressed

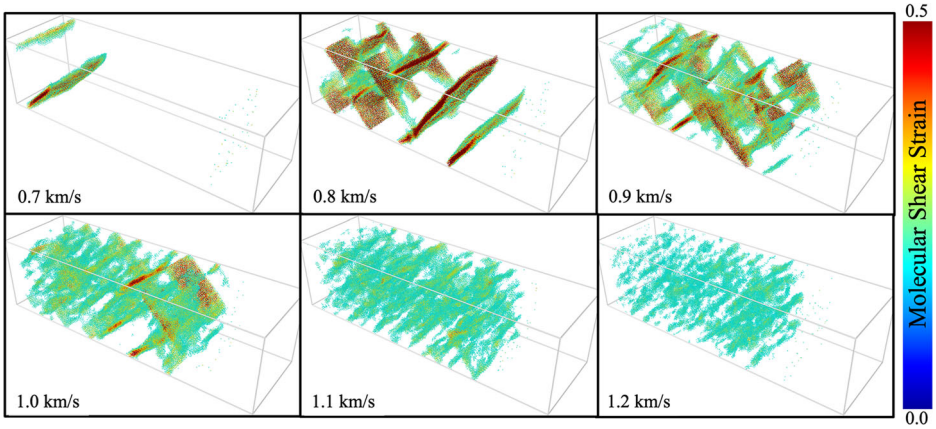

Fig. 4 | Molecular center of mass renderings at 50 ps after maximum compression for all particle velocities. Only molecules with a shear strain above 0.15 are rendered. Molecules are colored by shear strain.

Table 1 | Clustering results for a cluster analysis of the high shear strain molecules shown in Fig. 4

U_p	Pop.	N_{10}	N_{25}	N_{100}	C_{Max}	$C_{Max\%}$
0.7	16,145	3	1	1	15,401	95.3
0.8	92,627	7	1	1	88,787	95.8
0.9	109,401	40	2	1	103,225	94.3
1.0	107,424	85	8	4	98,328	91.5
1.1	97,802	193	37	18	80,091	81.9
1.2	52,902	372	102	65	13,854	26.2

Pop. is the total molecules used per frame. N_X is number of clusters with at least X molecules. C_{Max} is maximum cluster size, and $C_{Max\%}$ is the percentage of molecules in the max cluster.

plasticity cases show no differentiation between the sheared molecules and the rest of the system. While understanding the states in which plasticity occurs is paramount for understanding continued deformation and failure of materials in general, for energetic materials such as RDX, there is the further pertinence in that shear bands tend to generate a mechanochemical effect that can greatly alter the material's overall reactivity[21,35]. The high pressure lack of plastic deformation also has significant ramifications on the material strength and reactivity at its intended usage conditions.

To numerically assess the structure of the molecules with a shear strain greater than 0.15, as shown in Fig. 4, we perform a cluster analysis with a distance based cutoff of 6 Å, as implemented in OVITO[50]. These cutoffs include both sheared materials and shear embryos while excluding crystalline material. Table 1 shows the results for each of the particle velocities with the total number of molecules considered, the number of clusters with at least 10, 25, and 100 molecules, the size of the largest cluster, and what percentage of the considered molecules are in the largest cluster. While we conduct this analysis here on the 50 ps after holding the system at maximum compression frame, we find this to also be an extremely elucidating form of analysis for early time nucleation sites of shear bands in which we find similar results.

Starting with the maximum cluster size and percent, for the cases that shear band, the largest cluster is over 90% of all sheared atoms. This results from the various shear bands intersecting into a network to form one large cluster. In the 0.9 km/s case, a number of small ($N > 10$ molecules) clusters begin to form and do not become part of the shear banding network. By 1.1 km/s there are several hundred small clusters (embryos) with the largest cluster in the 1.2 km/s case only accounting for 26.2% of all sheared material, which is most likely an agglomeration of embryos in the cluster analysis. Supplementary Fig. 11 shows time history plots of the max cluster size and number of clusters larger than $N = 25$ for the initial shock. The latter shows the much larger increases for the non-shear banding cases, as well as a significant reduction in clusters after the material begins to release, showcasing the reversible (non-plastic) nature of the mechanism. As this release rejuvenates the crystal from embryo formation, but not from shear band nucleation and growth, it can be inferred that the embryo formation process exists in an elastic regime, where the transition from embryo to critical nucleus results in a plastic or non-reversible regime of deformation.

To better assess when a region has been shocked, we move to a 1 nm^3 3D Lagrangian binning, in which each bin only contains 3–4 molecules, resulting in little smoothing of the shear strain states. Figure 5 shows the average shear strain of each bin at 2.5 ps after the bin molecules experience the shockwave in the x-axis, with the shear strain after 50 ps held at maximum compression in the y-axis. For the weak shocks that shear band, little shearing occurs at early times and results in the data having a highly vertical trend. This lack of correlation is due to a majority of the shear bands growing from smaller nucleation sites, not shearing upon shock. In the cases of 1.1 and 1.2 km/s, the data follows a trend of the slope just greater than 1, showing almost no increase in shearing over time or any rearrangement in what areas are sheared more. Once the shear embryos

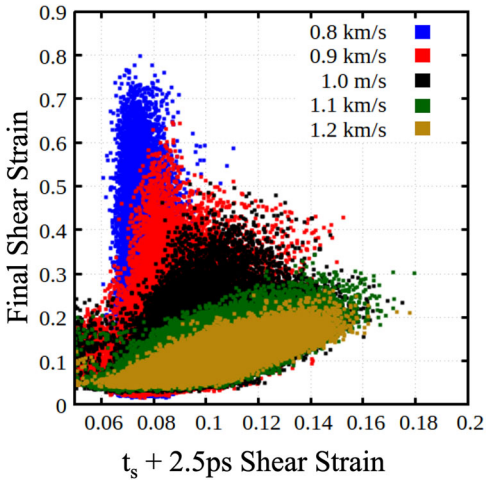

Fig. 5 | Correlations between the shear strain at 2.5 ps after a material section is shocked vs. the shear strain of that material at 50 ps after maximum compression. Each point represents a 1 nm^3 Lagrangian bin.

form, they are effectively stagnant until material release as no driver exists to push them toward forming a critical shearing nucleus. The result data trends have Pearson correlation coefficients of 0.083, 0.443, 0.674, 0.803, and 0.804 for 0.8, 0.9, 1.0, 1.1, and 1.2 km/s, respectively. Other than the initial nucleation sites, there is little to no correlation between the initial and final states of the shear banding case. However, the shear states of the higher pressure cases shows little temporal evolution, as the embryo formation mechanism lowers the deviatoric stress components, allowing the system to remain static in this state, resulting in a high pressure suppression of plasticity.

Discussion

In summary, through molecular dynamics simulations of the shock compression of the energetic material RDX, we find a high pressure mechanism for the suppression of plasticity via the over formation of shear embryos that never nucleate shear bands. Upon release of the compression state, these embryos heal and revert to the crystalline phase of the material, resulting in a reversible processes. This highly differs from lower pressure shocks in which plastic deformation results in significant shear band growth that remains upon release. Shock release rejuvenates the crystal from embryo formation, however, fully nucleated shear bands remain. From this it can be inferred that the embryo formation process exists in an elastic regime, where the transition from embryo to critical nucleus results in a plastic or non-reversible regime of deformation.

This phenomenon represents a process in which the increase of pressure transitions a material from a plastic back to an elastic regime, enabled by the high-strain rate and non-equilibrium nature of the process. In both cases, the deviatoric stress components are lowered, however, the non-plastic, high pressure mechanism results in a more rapid decay of the von Mises stress. Hence, the deformation mechanism that occurs at higher pressures supplants the shear banding mechanism and curtails its driving force prior to any plasticity.

A cluster analysis of sheared molecules shows the shear bands to be one large, interconnected network, whereas the high pressure system yields hundreds of small, independent clusters that do not significantly grow in size or shear magnitude over time, yet nevertheless lower the shear stress drivers for plasticity. Overall, the lack of high pressure shear banding is critical to RDX for both mechanical strength and mechanochemical effects on kinetics. Hence, future work will assess the broad nature of this mechanism in RDX for a variety of thermal, microstructure, and mechanical states, as well as non-shock high-strain rate conditions and its

prevalence in a variety of materials classes where high-strain rate plasticity is of great importance, such as polymer binders and materials for hypersonic applications. As experimental capabilities to study ultra-fast phenomena at the nanoscale to microscale continue to improve, processes such as nanoscale shear banding in single crystals will be able to be probed in tandem with both experiments and atomistic modeling to better understand the fundamental, underlying physics.

Methods

Molecular dynamics simulations

We use all-atom molecular dynamics using the LAMMPS package[51,52]. Atomic forces and energies for RDX are calculated with the non-reactive potential from Smith and Bharadwaj[53]. A 1.0 fs timestep was used in all simulations. Cells were constructed by replicating the alpha-RDX crystal structure along the [100], [010] and [001] directions, aligned with the x, y, and z Cartesian axis respectively, to lengths of 118.2 nm, 34.3 nm, and 31.8 nm ($30 \times 10 \times 10$ unit cells), respectively.

Prior to equilibration of the supercells, 5.0 nm of material was removed, by whole molecules, at either end of the x-direction to break periodicity and form a free surface. The system was then equilibrated for 500 ps at 300 K using a Nosé-Hoover thermostat[54], to allow breathing modes from the free surface creation to attenuate. Shock simulations were conducted using the reverse ballistic approach along the [100] direction[55]. The bottom 2.5 nm, by whole molecules, was held rigid to form an infinitely massive piston. When each shock reaches maximum compression, shock absorbing boundary conditions are applied to extend the simulation indefinitely[15,35,48]. All simulation analysis was conducted on a molecular center of mass framework. Additional methods and all specific analysis details are available in Supplementary Methods.

Data availability

The datasets used and/or analyzed during the current study available from the corresponding author on reasonable request.

Code availability

The underlying code for this study is entirely existing software, LAMMPS[52] and OVITO[50].

Received: 9 February 2024; Accepted: 4 July 2024;
Published online: 13 July 2024

References

1. Yan, N., Li, Z., Xu, Y. & Meyers, M. A. Shear localization in metallic materials at high strain rates. *Prog. Mater. Sci.* **119**, 100755 (2021).
2. Hu, X. et al. Amorphous shear bands in crystalline materials as drivers of plasticity. *Nat. Mat.* **22**, 1071–1077 (2023).
3. Wei, Q., Jia, D., Ramesh, K. & Ma, E. Evolution and microstru cture of shear bands in nanostructured Fe. *Appl. Phys. Lett.* **81**, 1240–1242 (2002).
4. Jonnalagadda, K., Karanjgaokar, N., Chasiotis, I., Chee, J. & Peroulis, D. Strain rate sensitivity of nanocrystalline Au films at room temperature. *Acta Mater.* **58**, 4674–4684 (2010).
5. Reddy, K. M., Liu, P., Hirata, A., Fujita, T. & Chen, M. Atomic structure of amorphous shear bands in boron carbide. *Nat. Commun.* **4**, 2483 (2013).
6. Chen, M., McCauley, J. W. & Hemker, K. J. Shock-induced localized amorphization in boron carbide. *Science* **299**, 1563–1566 (2003).
7. Hsiao, H.-W., Li, S., Dahmen, K. A. & Zuo, J.-M. Shear banding mechanism in compressed nanocrystalline ceramic nanopillars. *Phys. Rev. Mater.* **3**, 083601 (2019).
8. Moorcroft, R. L., Cates, M. E. & Fielding, S. M. Age-dependent transient shear banding in soft glasses. *Phys. Rev. Lett.* **106**, 055502 (2011).
9. Greer, A., Cheng, Y. & Ma, E. Shear bands in metallic glasses. *Mat. Sci. Eng. R.* **74**, 71–132 (2013).
10. Lewandowski, J. & Greer, A. Temperature rise at shear bands in metallic glasses. *Nat. Mat.* **5**, 15–18 (2006).
11. Bei, H., Xie, S. & George, E. P. Softening caused by profuse shear banding in a bulk metallic glass. *Phys. Rev. Lett.* **96**, 105503 (2006).
12. Pan, J., Ivanov, Y. P., Zhou, W., Li, Y. & Greer, A. Strain-hardening and suppression of shear-banding in rejuvenated bulk metallic glass. *Nature* **578**, 559–562 (2020).
13. Wang, N. et al. Spatial correlation of elastic heterogeneity tunes the deformation behavior of metallic glasses. *npj Comput. Mat.* **4**, 19 (2018).
14. Ding, J. & Ma, E. Computational modeling sheds light on structural evolution in metallic glasses and supercooled liquids. *npj Comput. Mat.* **3**, 9 (2017).
15. Cawkwell, M. J., Sewell, T. D., Zheng, L. & Thompson, D. L. Shock-induced shear bands in an energetic molecular crystal: application of shock-front absorbing boundary conditions to molecular dynamics simulations. *Phys. Rev. B* **78**, 1–13 (2008).
16. Wu, C.-Y. et al. Numerical and experimental investigation of capping mechanisms during pharmaceutical tablet compaction. *Powder Technol.* **181**, 121–129 (2008).
17. Cao, J. & Likhtman, A. E. Shear banding in molecular dynamics of polymer melts. *Phys. Rev. Lett.* **108**, 1–5 (2012).
18. Luo, H. et al. Plasticity without dislocations in a polycrystalline intermetallic. *Nat. Commun.* **10**, 3587 (2019).
19. Wu, P. & van der Giessen, E. Analysis of shear band propagation in amorphous glassy polymers. *Int. J. Solids Struct.* **31**, 1493–1517 (1994).
20. Huang, J. & Gray III, G. Microband formation in shock-loaded and quasi-statically deformed metals. *Acta Metall.* **37**, 3335–3347 (1989).
21. Kroonblawd, M. P. & Fried, L. E. High explosive ignition through chemically activated nanoscale shear bands. *Phys. Rev. Lett.* **124**, 206002 (2020).
22. Johnson, B. P., Zhou, X., Ihara, H. & Dlott, D. D. Observing hot spot formation in individual explosive crystals under shock compression. *J. Phys. Chem. A* **124**, 4646–4653 (2020).
23. Bassett, W. P. & Dlott, D. D. Shock initiation of explosives: temperature spikes and growth spurts. *Appl. Phys. Lett.* **109**, 091903 (2016).
24. Ravasio, A. et al. Metallization of shock-compressed liquid ammonia. *Phys. Rev. Lett.* **126**, 025003 (2021).
25. Sharma, S. M. et al. Real-time observation of stacking faults in gold shock compressed to 150 gpa. *Phys. Rev. X* **10**, 011010 (2020).
26. Hwang, H. et al. Subnanosecond phase transition dynamics in laser-shocked iron. *Sci. Adv.* **6**, eaaz5132 (2020).
27. Armstrong, M. R. et al. Ultrafast shock synthesis of nanocarbon from a liquid precursor. *Nat. Commun.* **11**, 1–7 (2020).
28. Wang, X. et al. The laser shock station in the dynamic compression sector. I. *Rev. Sci. Instrum.* **90**, 053901 (2019).
29. Rygg, J. R. et al. X-ray diffraction at the National Ignition Facility. *Rev. Sci. Instrum.* **91**, 043902 (2020).
30. Armstrong, M. R. et al. Highly ordered graphite (HOPG) to hexagonal diamond (lonsdaleite) phase transition observed on picosecond time scales using ultrafast x-ray diffraction. *J. Appl. Phys.* **132**, 055901 (2022).
31. Hamilton, B. W., Sakano, M. N., Li, C. & Strachan, A. Chemistry under shock conditions. *Ann. Rev. Mater. Res.* **51**, 101–130 (2021).
32. Manaa, M. R. Shear-induced metallization of triamino-trinitrobenzene crystals. *Appl. Phys. Lett.* **83**, 1352–1354 (2003).
33. Gilman, J. J. Shear-induced metallization. *Philos. Mag. B* **67**, 207–214 (1993).
34. Gilman, J. J. Chemical reactions at detonation fronts in solids. *Philos. Mag. B* **71**, 1057–1068 (1995).
35. Hamilton, B. W., Kroonblawd, M. P., Li, C. & Strachan, A. A hotspot's better half: non-equilibrium intra-molecular strain in shock physics. *J. Phys. Chem. Lett.* **12**, 2756–2762 (2021).

36. Hamilton, B. W., Kroonblawd, M. P. & Strachan, A. The potential energy hotspot: effects from impact velocity, defect geometry, and crystallographic orientation. *J. Phys. Chem. C* **126**, 3743–3755 (2022).
37. Hamilton, B. W., Kroonblawd, M. P., Macatangay, J., Springer, H. K. & Strachan, A. Intergranular hotspots: a molecular dynamics study on the influence of compressive and shear work. *J. Phys. Chem. C* **127**, 9858–9870 (2023).
38. Wood, M. A., Cherukara, M. J., Kober, E. M. & Strachan, A. Ultrafast chemistry under nonequilibrium conditions and the shock to deflagration transition at the nanoscale. *J. Phys. Chem. C* **119**, 22008–22015 (2015).
39. Frey, R. B. The initiation of explosive charges by rapid shear. In *Proceedings of the 7th Symposium (International) on Detonation*, 36–42 (1982).
40. Hamilton, B. W., Kroonblawd, M. P. & Strachan, A. Extemporaneous mechanochemistry: shockwave induced ultrafast chemical reactions due to intramolecular strain energy. *J. Phys. Chem. Lett.* **13**, 6657–6663 (2022).
41. Hamilton, B. W. & Strachan, A. Many-body mechanochemistry: intramolecular strain in condensed matter chemistry. *Phys. Rev. Mater.* **7**, 075601 (2023).
42. Kroonblawd, M. P. & Goldman, N. Mechanochemical formation of heterogeneous diamond structures during rapid uniaxial compression in graphite. *Phys. Rev. B* **97**, 184106 (2018).
43. Hamilton, B. W. & Germann, T. C. Interplay of mechanochemistry and material processes in the graphite to diamond phase transformation. *J. Phys. Chem. Lett.* **14**, 8584–8589 (2023).
44. Davis, D. A. et al. Force-induced activation of covalent bonds in mechanoresponsive polymeric materials. *Nature* **459**, 68–72 (2009).
45. Hamilton, B. W. & Strachan, A. Rapid activation of non-oriented mechanophores via shock loading and spallation. *Phys. Rev. Mater.* **7**, 045601 (2023).
46. Izvekov, S. & Rice, B. M. Bottom-up coarse-grain modeling of plasticity and nanoscale shear bands in α-rdx. *J. Chem. Phys.* **155**, 064503 (2021).
47. Izvekov, S. & Rice, B. M. Microscopic mechanism of nanoscale shear bands in an energetic molecular crystal (α-rdx): a first-order structural phase transition. *Phys. Rev. B* **106**, 104109 (2022).
48. Zhao, S., Germann, T. C. & Strachan, A. Atomistic simulations of shock-induced alloying reactions in NiAl nanolaminates. *J. Chem. Phys.* **125**, 164707 (2006).
49. Dreger, Z. A. & Gupta, Y. M. Phase diagram of hexahydro-1, 3, 5-trinitro-1, 3, 5-triazine crystals at high pressures and temperatures. *J. Phys. Chem. A* **114**, 8099–8105 (2010).
50. Stukowski, A. Visualization and analysis of atomistic simulation data with ovito—the open visualization tool. *Model. Simul. Mater. Sci. Eng.* **18**, 015012 (2009).
51. Plimpton, S. Fast parallel algorithms for short-range molecular dynamics. *J. Comput. Phys.* **117**, 1–19 (1995).
52. Thompson, A. P. et al. LAMMPS—a flexible simulation tool for particle-based materials modeling at the atomic, meso, and continuum scales. *Comput. Phys. Commun.* **271**, 108171 (2022).
53. Smith, G. D. & Bharadwaj, R. K. Quantum chemistry based force field for simulations of HMX. *J. Phys. Chem. B* **103**, 3570–3575 (1999).
54. Nosé, S. A unified formulation of the constant temperature molecular dynamics methods. *J. Chem. Phys.* **81**, 511–519 (1984).
55. Holian, B. L. & Straub, G. K. Molecular dynamics of shock waves in three-dimensional solids: transition from nonsteady to steady waves in perfect crystals and implications for the Rankine-Hugoniot conditions. *Phys. Rev. Lett.* **43**, 1598–1600 (1979).

Acknowledgements

The authors thank Marc Cawkwell for useful discussions regarding RDX shear banding and phase transformations. Funding for this project was provided by the Director's Postdoctoral Fellowship program at Los Alamos National Laboratory, project LDRD 20220705PRD1. Partial funding was provided by the Advanced Simulation and Computing Physics and Engineering Models project (ASC-PEM). This research used resources provided by the Los Alamos National Laboratory (LANL) Institutional Computing Program. This work was supported by the U.S. Department of Energy (DOE) through LANL, which is operated by Triad National Security, LLC, for the National Nuclear Security Administration of the U.S. Department of Energy (Contract No. 89233218CNA000001). Approved for Unlimited Release LA-UR-21177.

Author contributions

B.W.H. and T.C.G. conceived the study. B.W.H. conducted all simulations and wrote the manuscript. T.C.G. helped with devising analysis techniques. B.W.H. and T.C.G. contributed to discussions and revisions of the results and manuscript.

Competing interests

The authors declare no competing interests.

Additional information

Supplementary information The online version contains supplementary material available at https://doi.org/10.1038/s41524-024-01348-w.

Correspondence and requests for materials should be addressed to Brenden W. Hamilton.